Exotic nuclei and drip lines

- Unstable vs. stable nuclei: neutron-rich and proton-rich systems
- Limit of nuclear stability and definition of drip lines

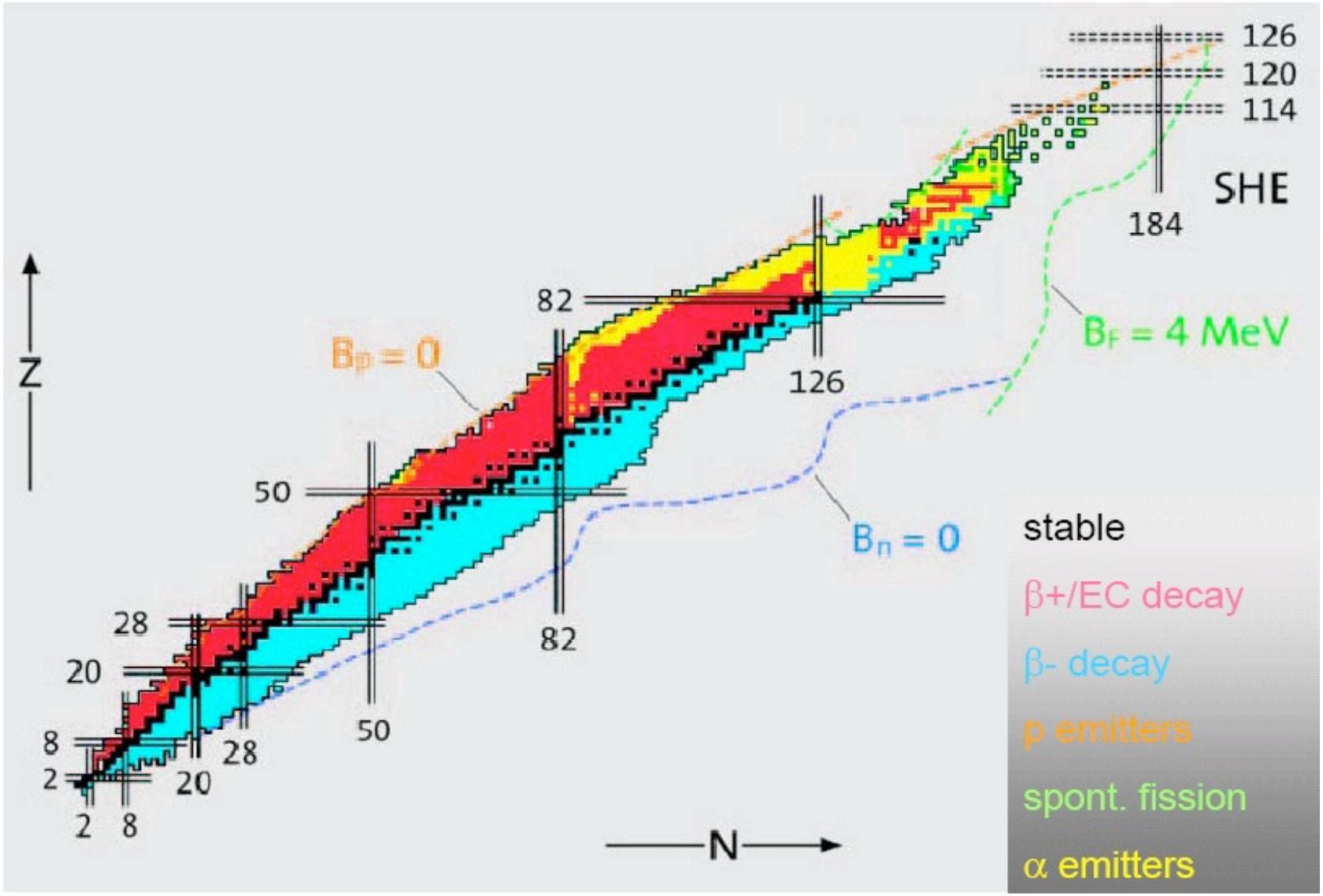

From: Exotic Nuclei, J. Enders, TU Darmstadt, Summer 2003

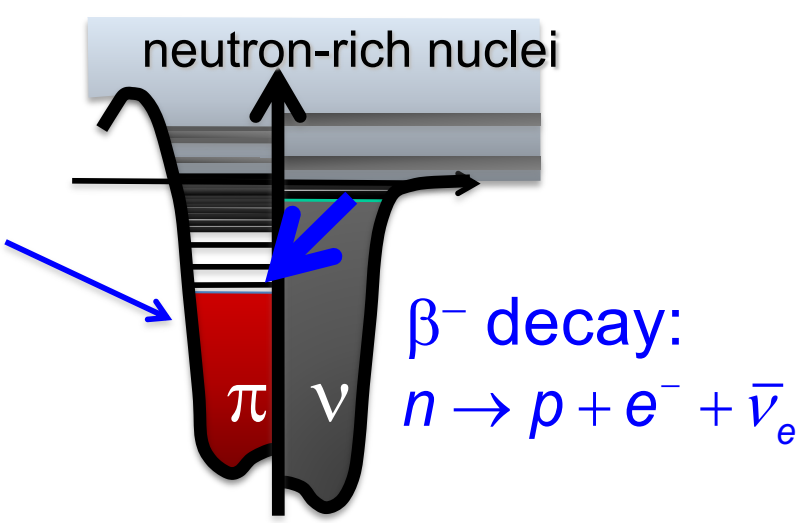

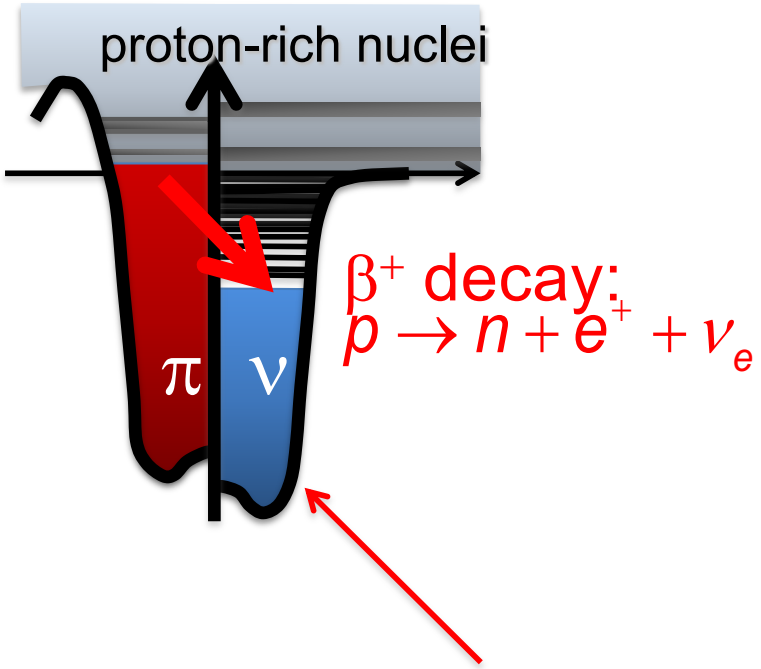

- Nuclei that are neutron- or proton-rich undergo β-decay.
- Although unstable, these nuclei exist as bound systems. The limit of nuclear stability with respect to the strong interaction is the **drip line**. Neutron and proton **drip lines** are sketched in the previous slide but they are only partially known.

Lifetimes for beta-decay can be quite long and unstable nuclei can nonetheless be studied nowadays using RIB (Radioactive Isotope Beam) facilities.

We meet, by further increasing (or decreasing) N-Z the neutron (proton) drip line. These are defined as the limits beyond which the systems are unstable against particle emission. In the case of neutrons, the one-neutron or two-neutron separation energies (S_n = BE(N)-BE(N-1) or S_{2n}) become zero.

In certain cases, systems beyond the drip lines can be studied: for instance, if the lifetime is relatively long due to the fact that the extra neutron (or proton) has a resonant state available. But this is not the rule !

Discovering new exotic isotopes

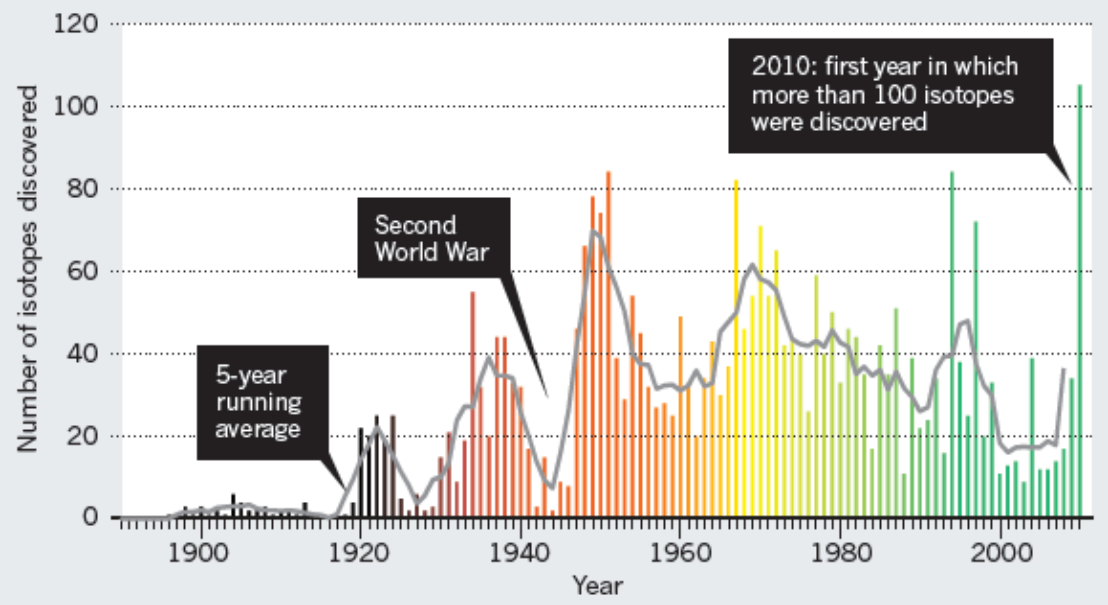

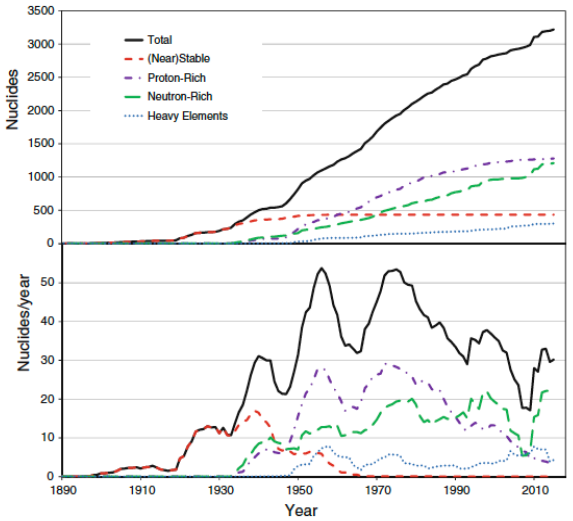

M. Thoennessen, B. Sherrill, Nature 473, 25 (2011).

http://www.nscl.msu.edu/~thoennes/isotopes/

In this web page new discovered isotopes are reported.
Updated to 2020.

2022 UPDATE OF THE DISCOVERIES OF NUCLIDES

M. THOENNESSEN

Facility for Rare Isotope Beams and
Department of Physics & Astronomy
Michigan State University
East Lansing, Michigan 48824, USA
thoennessen@nscl.msu.edu

Received Day Month Year
Revised Day Month Year

The 2022 update of the discovery of nuclide project is presented. It is the first update in four years, and 36 new nuclides were observed for the first time during 2019-2022. Isotopes that have so far only been published in conference proceedings or internal reports are also listed.

Keywords: Discovery of nuclides; discovery of isotopes

PACS numbers: 21.10.-k, 29.87.+g

1. Introduction

This is the seventh update of the isotope discovery project which was originally published in a series of papers in Atomic Data and Nuclear Data Tables from 2009 through 2013 (see for example the first[1] and last[2] papers). Two summary papers were published in 2012 and 2013 in Nuclear Physics News[3] and Reports on Progress in Physics,[4] respectively, followed by annual updates in 2014,[5] 2015,[6] 2016,[7] 2017,[8] 2018,[9] and 2019.[10] No updates were published since then because of the small number of isotopes discovered during these years. In 2016 a description of the discoveries from a historical perspective was published in the book "The Discovery of Isotopes – A complete Compilation".[11]

Table 1. New nuclides reported in 2019. The nuclides are listed with the first author, submission date, and reference of the publication, the laboratory where the experiment was performed, and the production method (FE = fusion evaporation, SB = secondary beams).

Nuclide(s)	First Author	Subm. Date	Ref.	Laboratory	Type
^{11}O	T. B. Webb	12/20/2018	12	MSU	SB
^{220}Np	Z. Y. Zhang	1/9/2019	13	Lanzhou	FE
^{165}Pt, ^{170}Hg	J. Hilton	5/13/2019	14	Jyväskylä	FE
^{68}Br	K. Wimmer	5/15/2019	15	RIKEN	SB
^{31}K	D. Kostyleva	5/22/2019	16	GSI	SB

Table 2. New nuclides reported in 2020. The nuclides are listed with the first author, submission date, and reference of the publication, the laboratory where the experiment was performed, and the production method (FE = fusion evaporation).

Nuclide(s)	First Author	Subm. Date	Ref.	Laboratory	Type
^{244}Md	J. L. Pore	1/31/2020	18	Berkeley	FE
^{235}Cm	J. Khuyagbaatar	2/26/2020	21	GSI	FE
^{222}Np	L. Ma	5/8/2020	22	Lanzhou	FE
^{211}Pa	K. Auranen	6/23/2020	23	Jyväskylä	FE

Table 3. New nuclides reported in 2021. The nuclides are listed with the first author, submission date, and reference of the publication, the laboratory where the experiment was performed, and the production method (PF = projectile fragmentation, FE = fusion evaporation, SB = secondary beams, SP = spallation).

Nuclide(s)	First Author	Subm. Date	Ref.	Laboratory	Type
^{101}Br, ^{102}Kr, ^{105}Rb, ^{106}Rb, ^{108}Sr, ^{110}Y, ^{111}Y, ^{114}Zr, ^{117}Nb	T. Sumikama	7/6/2020	24	RIKEN	PF
^{280}Ds	A. Samark-Roth	11/16/2020	25	GSI	FE
^{13}F	R. J. Charity	11/16/2020	26	MSU	SB
^{249}No	J. Khuyagbaatar	1/3/2021	27	GSI	FE
^{214}U	Z. Y. Zhang	1/15/2021	28	Lanzhou	FE
^{150}Yb	S. Beck	4/13/2021	29	TRIUMF	SP
^{18}Mg	Y. Jin	8/30/2021	30	MSU	SB

Table 4. New nuclides reported in 2022. The nuclides are listed with the first author, submission date, and reference of the publication, the laboratory where the experiment was performed, and the production method (PF = projectile fragmentation, FE = fusion evaporation).

Nuclide(s)	First Author	Subm. Date	Ref.	Laboratory	Type
^{149}Lu	K. Auranen	12/15/2021	35	Jyväskylä	FE
^{207}Th	H. B. Yang	2/7/2022	36	Lanzhou	FE
^{264}Lr	Yu. Ts. Oganessian	3/11/2022	37	Dubna	FE
^{166}Pm, ^{168}Sm, ^{170}Eu, ^{172}Gd	G. G. Kiss	4/29/2022	38	RIKEN	PF
^{204}Ac	M. H. Huang	6/27/2022	39	Lanzhou	FE
^{251}Lr	T. Huang	6/30/2022	40	Argonne	FE
^{39}Na	D. S. Ahn	9/8/2022	41	RIKEN	PF
^{286}Mc	Yu. Ts. Oganessian	10/10/2022	42	Dubna	FE

Model extrapolations to the drip line

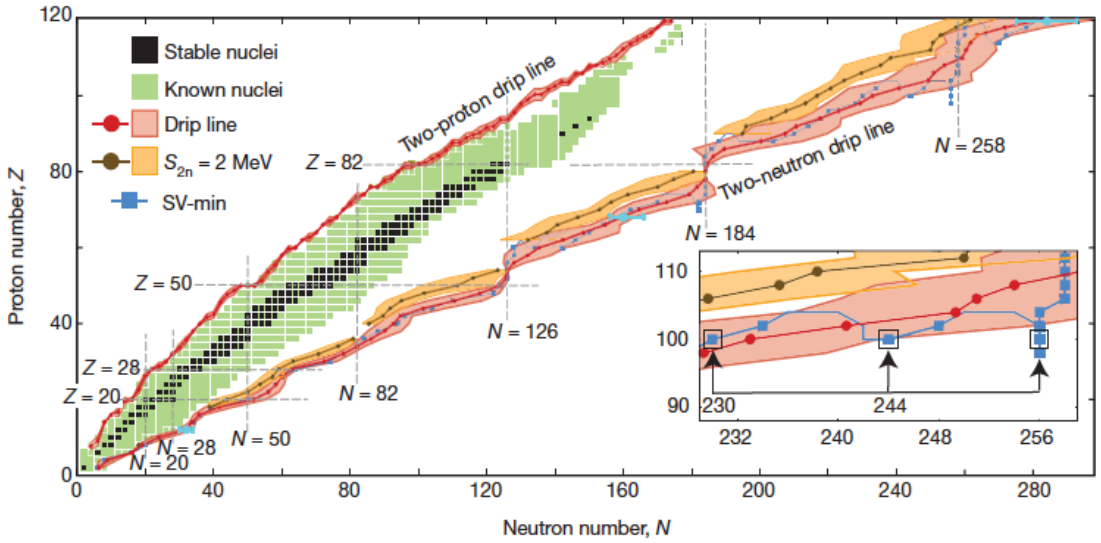

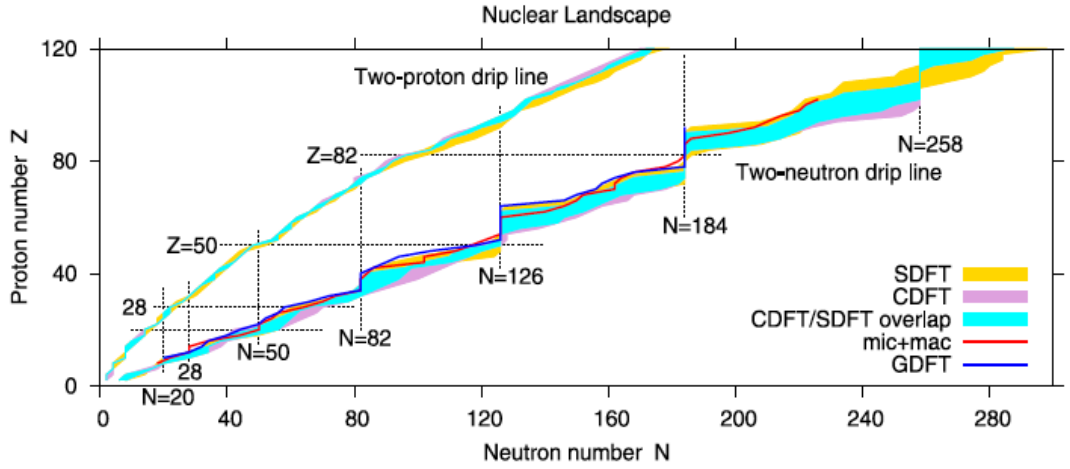

Fig. 4. The comparison of the uncertainties in the definition of two-proton and two-neutron drip lines obtained in CDFT and SDFT. The shaded areas are defined by the extremes of the predictions of the corresponding drip lines obtained with different parametrizations. The blue shaded area shows the area where the CDFT and SDFT results overlap. Non-overlapping regions are shown by dark yellow and plum colors for SDFT and CDFT, respectively. The results of the SDFT calculations are taken from the supplement to Ref. [2]. The two-neutron drip lines obtained by microscopic + macroscopic (FRDM [3]) and Gogny D1S DFT [5] calculations are shown by red and blue lines, respectively. (For interpretation of the references to color in this figure legend, the reader is referred to the web version of this Letter.)

J. Erler *et al.*, Nature 486, 509 (2012) - SEDF

A.V. Afanasjev *et al.*, Phys. Lett. B726, 680 (2013) - CEDF

In the previous figures:

black dots correspond to stable nuclei: i.e., infinite lifetime.

Stable nuclei can be found around the so-called stability line.

First problems: for each A (that is, for each isobaric chain), which is the nucleus with largest binding energy ? And how does this evolve if we move towards right (left) in the previous figure, that is, if we move increasing (decreasing) (N-Z) ?

The solution of the first problem can be attempted by using the well-known Bethe-Weiszäcker mass formula. We take this problem from [Hey94].

$$M(A,Z)c^2 = Zm_pc^2 + (A-Z)m_nc^2 \\ -a_VA + a_SA^{2/3} + a_A(A-2Z)^2A^{-1} \\ +a_CZ(Z-1)A^{-1/3} + \\ \text{pairing term} : 0, \pm\delta. \qquad (1)$$

If we wish, for each A, the nucleus with the lowest mass, or largest binding energy, we must re-write the above equation (neglecting the pairing term) as

$$M(A,Z)c^2 = f(A) + pZ + qZ^2, \qquad (2)$$

where the constants p and q can be easily obtained, and then

$$\frac{\partial}{\partial Z}Mc^2 = 0 \qquad (3)$$

is solved for

$$Z_0 = \frac{-p}{2q}. \qquad (4)$$

We can obtain Z_0 (value of Z corresponding to the lowest mass) by replacing the values of p and q and then multiplying the numerator and denominator by $A/8a_A$:

$$Z_0 = \frac{\frac{A}{2} + (m_n - m_p)c^2\frac{A}{8a_A} + \frac{a_C A^{2/3}}{8a_A}}{1 + \frac{1}{4}\frac{a_C}{a_A}A^{2/3}}. \qquad (1)$$

In the numerator, the second and third terms are negligible with respect to the first one. This leads to

$$Z_0 = \frac{\frac{A}{2}}{1 + 0.0077A^{2/3}}. \qquad (2)$$

Values:

a_V=15.85 MeV
a_S=18.34 MeV
a_C=0.71 MeV
a_A=23.21 MeV

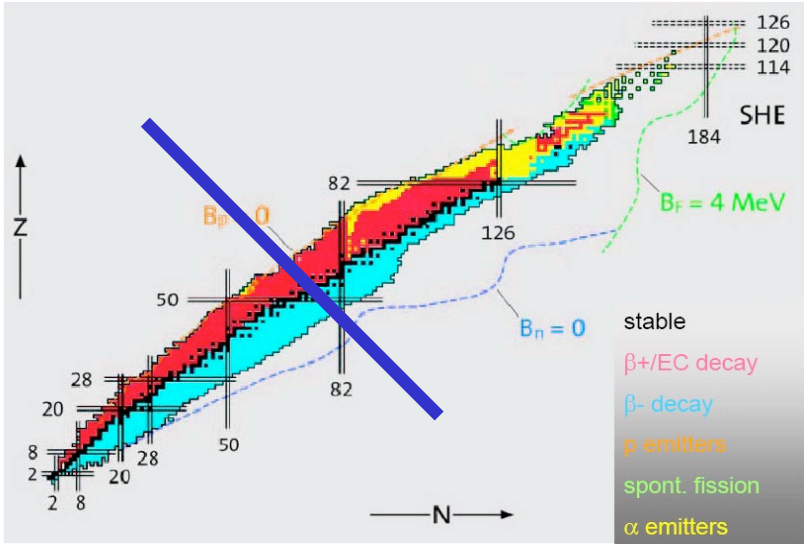

The blue line represents constant A: for A=120 we meet Z_0 close to 50 (i.e., Sn).

Gamow-Teller beta decay and isospin impurity in nuclei near the proton drip line

I. Hamamoto[1,2] and H. Sagawa[1,3]
[1]*Department of Physics, Faculty of Science, The University of Tokyo, Hongo 7-3-1, Bunkyo-ku, Tokyo 113, Japan*
[2]*Department of Mathematical Physics, Lund Institute of Technology, Lund, Sweden**
[3]*Center for Mathematical Sciences, University of Aizu, Aizu-Wakamatsu, Fukushima 965, Japan**
(Received 4 May 1993)

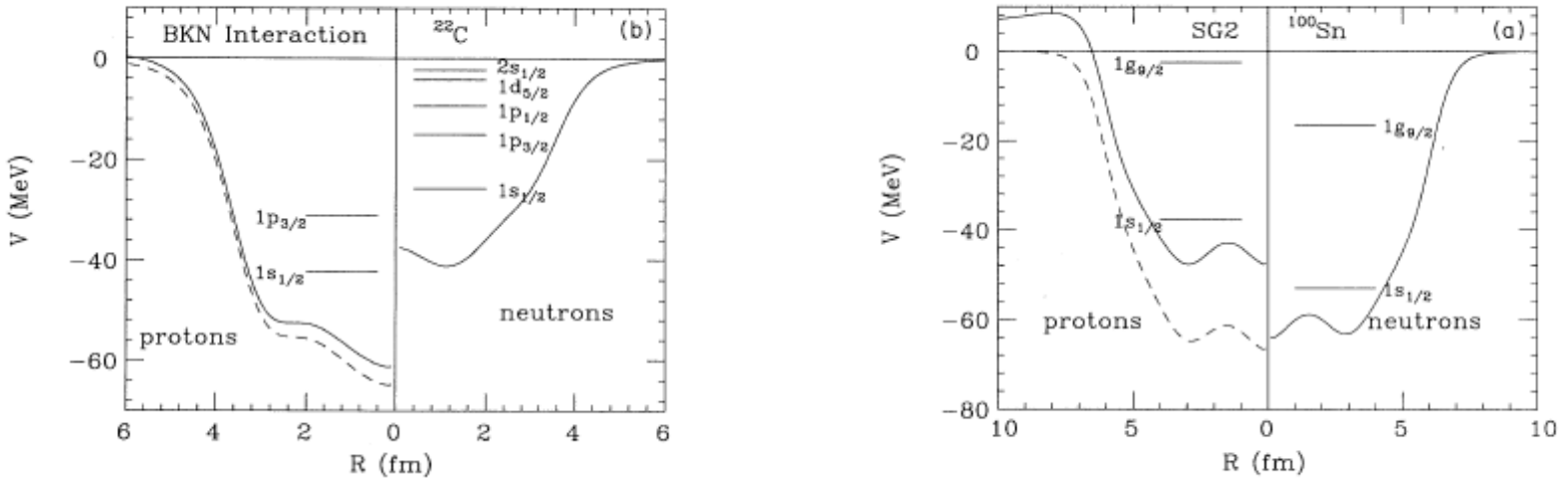

FIG. 1. HF potentials of ^{100}Sn (a) and ^{22}C (b). The Skyrme interactions, SG2 and BKN, are used for ^{100}Sn and ^{22}C, respectively. The dashed (solid) lines for protons show the HF potential without (with) the Coulomb potential. Since the HF calculation is performed with the Coulomb potential, there is a small difference between the dashed line for protons and the solid line for neutrons in ^{100}Sn. In ^{100}Sn only the lowest-lying one-particle level ($=1s_{1/2}$) and the highest occupied level ($=1g_{9/2}$) are shown, while in ^{22}C all occupied one-particle levels are denoted.

Neutron-rich and proton rich nuclei in HF with effective forces:

Reminder: the pp and nn force is active only in the T=1 channel (on average, not so much attractive), whereas the pn force is active also in the T=0 channel which provides stronger attraction. This is known from the existence of the deuteron as a bound system, and the non-existence of the di-neutron.

Therefore, neutrons feel more the proton attraction than the attraction of the other neutrons. In a system with increasing N-Z, the neutrons become much less bound with respect to the protons.

For analogous reasons, in a system which is neutron deficient, the protons become much less bound with respect to the neutrons.

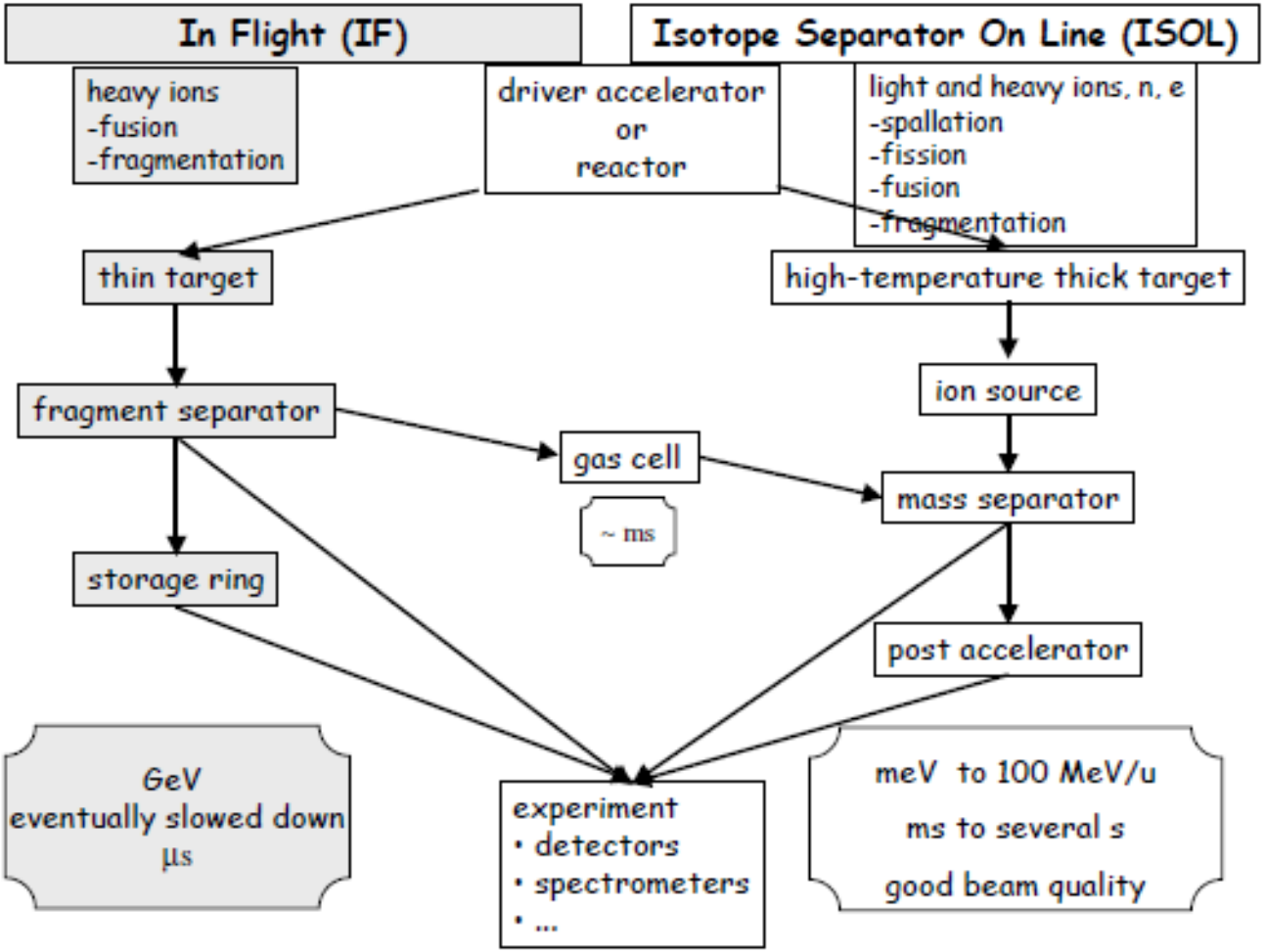

The Why and How of Radioactive-Beam Research

Mark Huyse

University of Leuven, Instituut voor Kern- en Stralingsfysica,
Celestijnenlaan 200 D, 3001 Leuven, Belgium

Measurements of masses and densities of radioactive nuclei

• Masses (or equivalently binding energies) can be measured with good accuracy by means of mass spectrometry.

• The difference between stable and unstable nuclei comes at the level of density measurements. In the case of stable nuclei, electron scattering has been the main source of information. The electromagnetic interaction is known, and this has allowed to interpret the data since the differential elastic cross section for electron scattering is expected to be the Mott cross section (corresponding to the diffusion on a point charge) multiplied by the form factor $F(q^2)$ squared, that is, the Fourier transform of the nuclear charge density,

$$\frac{d\sigma}{d\Omega} = \left(\frac{d\sigma}{d\Omega}\right)_{\text{Mott}} |F(q^2)|^2$$

$$\rho_{\text{charge}}(r) = \frac{1}{2\pi^2 r}\int_0^\infty F(q^2) sin(qr) q dq$$

In the case of unstable nuclei, this is not possible. Sizes and densities have been measured using hadron scattering → with the associated uncertainities !

Chapter 3

SIZES AND ENERGIES OF EXOTIC NUCLEI

3.1 Introduction

The first experiments with unstable nuclear beams were designed to measure the nuclear sizes, namely the matter distribution of protons and neutrons. For stable nuclei such experiments are best accomplished with electron beams, which probe the nuclear charge (proton) distribution. Electron scattering experiments with unstable beams can only be performed in an electron-nucleus collider. Such machines are not yet available. The easiest solution is to measure the *interaction cross section* in collisions of unstable beams with a fixed target nucleus.

The interaction cross section is defined as the cross section for the change of proton and/or neutron number in the incident nucleus. To extract the *interaction radii* of the radioactive secondary beam nuclei, one has assumed that it can be expressed as [1]

$$\sigma_I(P,T) = \pi\,[R_I(P) + R_I(T)]^2 \qquad (3.1)$$

where $R_I(P)$ and $R_I(T)$ are the interaction radii of the projectile and the target nuclei, respectively. $R_I(T)$ can be obtained from σ_I in collisions between identical nuclei, while $R_I(P)$ can be obtained by measuring σ_I for different targets T [1].

The above equation assumes a separability of the projectile and target radius. This hypotheses has been tested by Tanihata and collaborators [1]. As an example, the interaction radii R_I for Li and Be isotopes have been obtained using three different targets. The results are shown in Fig. 1.

In Table 3.1 we show in the first column the interaction radii of several nuclei obtained with this technique [1]. In the last column the root mean charge radius of some nuclei obtained by electron scattering, $R^e_{\rm rms}$, are also shown. One observes that $R^e_{\rm rms}$ is almost constant for $A \geq 6$, while R_I increases with A. One can show that this difference is due to the definitions of the two radii but not due to a difference between the charge and the matter distributions. To prove it we use an eikonal calculation for the cross sections. The *rms* radius of the matter density can be determined independently of the assumed model density functions. The eikonal approximation and its use in nuclear physics is presented in Chapters 1 and 2.

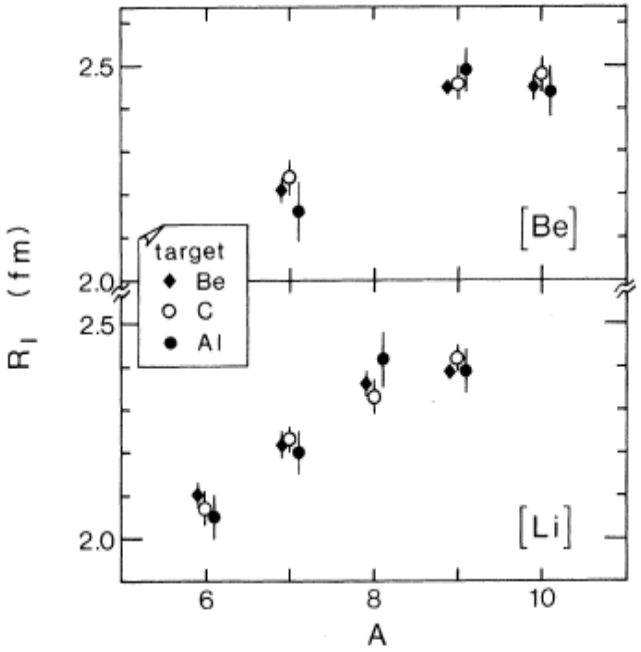

FIG. 1. R_I for Li and Be isotopes. The values obtained by three different targets agree with each other showing the separability of projectile and target R_I.

Table 3.1: cf. next page

TABLE II. Interaction nuclear radii and rms radii, in fermis.

		e scat.	Gaussian	Harmonic oscillator		
	R_I	$R^e_{\rm rms}$	$R^G_{\rm rms}$	$R^m_{\rm rms}$ [a]	$R^c_{\rm rms}$ [a]	$R^n_{\rm rms}$ [a]
^{4}He	1.41 ± 0.03	1.67 ± 0.01	1.72 ± 0.06	1.72 ± 0.06	1.72 ± 0.06	1.72 ± 0.06
^{6}He	2.18 ± 0.02		2.75 ± 0.04	2.73 ± 0.04	2.46 ± 0.04	2.87 ± 0.04
^{8}He	2.48 ± 0.03		2.70 ± 0.03	2.69 ± 0.03	2.33 ± 0.03	2.81 ± 0.03
^{6}Li	2.09 ± 0.02	2.56 ± 0.10	2.54 ± 0.03	2.54 ± 0.03	2.54 ± 0.03	2.54 ± 0.03
^{7}Li	2.23 ± 0.02	2.41 ± 0.10	2.50 ± 0.03	2.50 ± 0.03	2.43 ± 0.03	2.54 ± 0.03
^{8}Li	2.36 ± 0.02		2.51 ± 0.03	2.51 ± 0.03	2.41 ± 0.03	2.57 ± 0.03
^{9}Li	2.41 ± 0.02		2.43 ± 0.02	2.43 ± 0.02	2.30 ± 0.02	2.50 ± 0.02
^{11}Li	3.14 ± 0.16		3.27 ± 0.24	3.27 ± 0.24	3.03 ± 0.24	3.36 ± 0.24
^{7}Be	2.22 ± 0.02		2.48 ± 0.03	2.48 ± 0.03	2.52 ± 0.03	2.41 ± 0.03
^{9}Be	2.45 ± 0.01	2.52 ± 0.01	2.49 ± 0.01	2.50 ± 0.01	2.47 ± 0.01	2.53 ± 0.01
^{10}Be	2.46 ± 0.03		2.38 ± 0.02	2.39 ± 0.02	2.34 ± 0.02	2.43 ± 0.02
^{12}C	2.61 ± 0.02	2.45 ± 0.01	2.40 ± 0.02	2.43 ± 0.02	2.43 ± 0.02	2.43 ± 0.02

[a]Superscripts *m*, *c*, and *n* indicate the nuclear matter, the charge, and the neutron matter distributions, respectively.

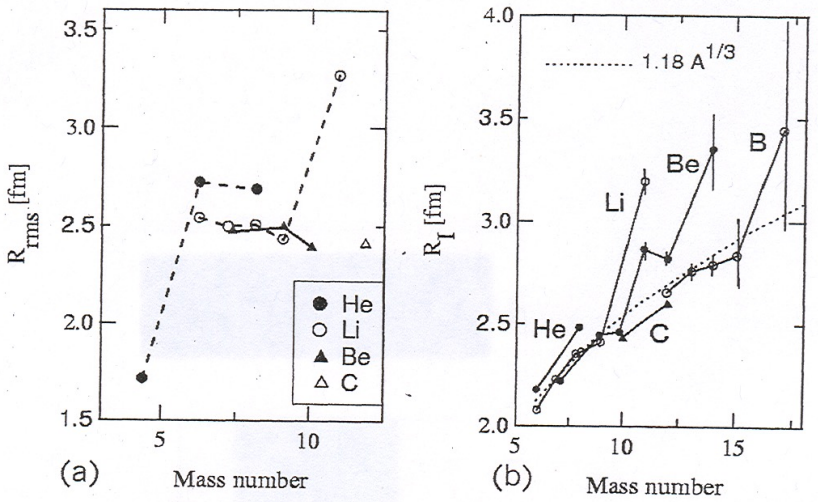

Figure 5 (a) Rms radii for the neutron-rich isotopes He, Li, Be, and C. (b) The matter density radii of several light nuclei compared to the trend $R \sim 1.18\ A^{1/3}$ fm (dashed line) for normal nuclei. The solid lines are guide to the eyes.

The wavefunction of a loosely-bound nucleon (as in the case of the deuteron) extends far beyond the nuclear potential. For large distances the wavefunction behaves as an Yukawa function,

$$R(r)/r \sim \frac{e^{-\eta r}}{r} \tag{3.38}$$

where $(\hbar\eta)^2 = 2mB$, with B equal to the binding energy and m the nucleon mass. Thus, the smaller the value of B is, the more the wavefunction extends to larger $r's$. Thus the "halo" in an exotic unstable nuclei, like ^{11}Li, is a simple manifestation of the weak binding energy of the last nucleons. What is not as trivial is to know why ^{6}He and ^{11}Li are bound while ^{5}He and ^{10}Li are not. We will continue this discussion later.

Abnormally large radii were also found for other light neutron-rich nuclei [7] as shown in figure 5(b).

The matter density radii of these nuclei do not follow the commonly observed trend $R \sim 1.18\ A^{1/3}$ fm of normal nuclei. Thus the halo seems to be a common feature of loosely-bound neutron-rich nuclei. In Table 3.3 we list the spin, parities and mass number of some light neutron-rich nuclei. The separation energy of one neutron (S_n) and of two neutrons (S_{2n}) are also shown. One observes that the two-neutron separation energies of ^{11}Li, ^{14}Be and ^{17}B are very small and are responsible for large matter radii of these nuclei, as seen in figure 5(b). A nuclear chart with the halo nuclei is shown in Figure 6.

Examples: ^{11}Li and ^{11}Be (courtesy: T. Nakamura)

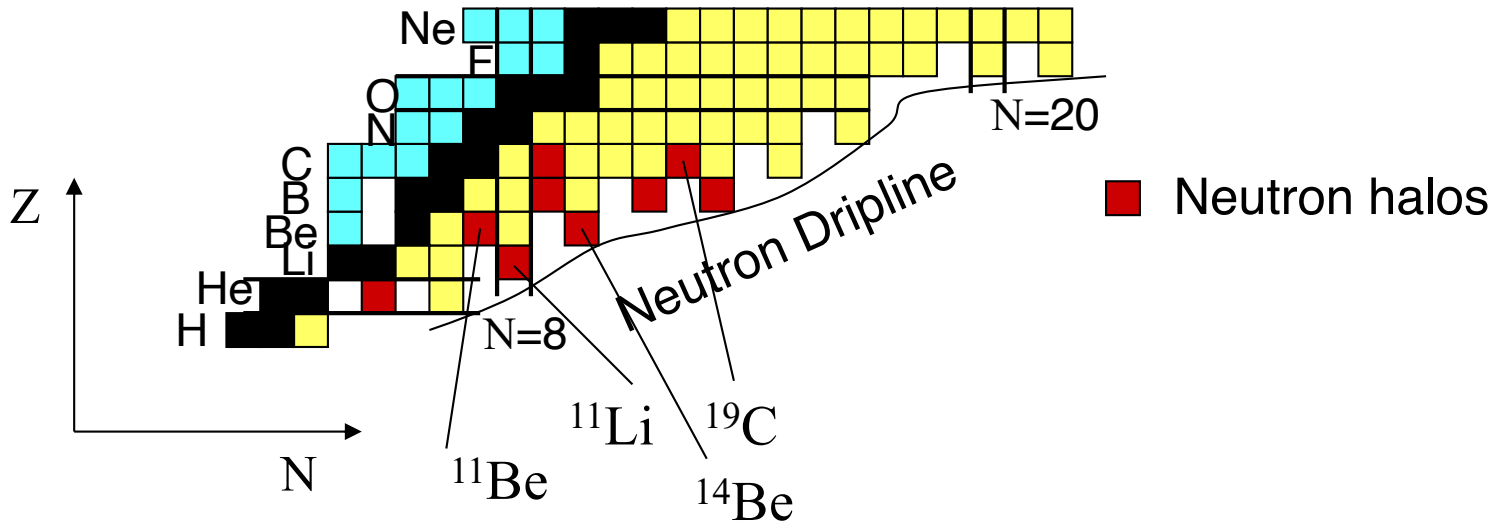

1n halo nucleus

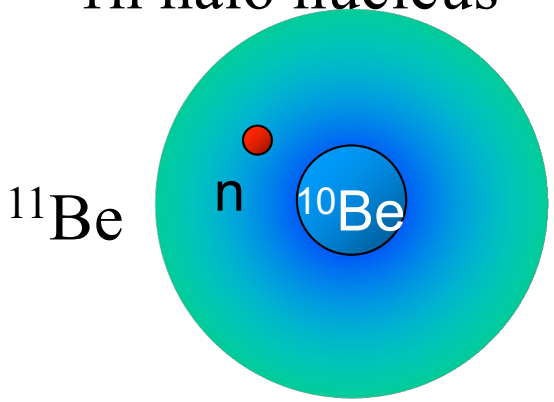

S_n=504 keV

2n halo nucleus

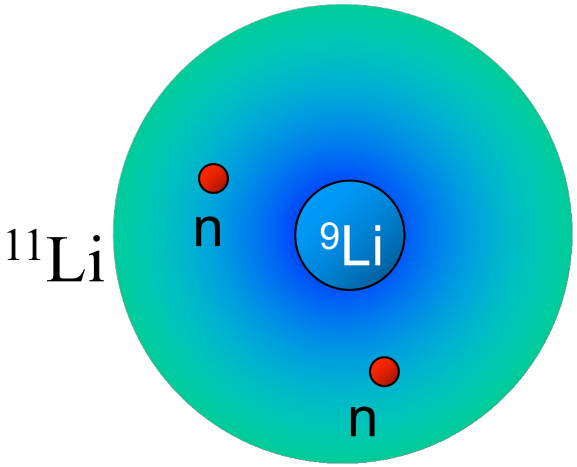

S_{2n}=300 keV

In oder to understand the correlation between the appearance of a halo and the small binding energy of a neutron, we use a simple model (square well). It is well known that in this case, namely

$$V = -V_0 (r < r_0) \qquad = 0 (r > r_0), \qquad (1)$$

the radial Schrödinger equation takes the form

$$-\frac{\hbar^2}{2\mu}\frac{d^2u}{dr^2} + V_{\text{eff}}(r)u = Eu, \qquad (2)$$

where μ is the reduced mass and the effective potential includes the centrifugal term. For ℓ=0, the centrifugal barrier is absent and the solution for negative energy is

$$\begin{aligned} u(r) &= Asin(kr), \quad \text{for } r < r_0 \\ &= Be^{-\eta r}, \quad \text{for } r < r_0, \end{aligned} \qquad (3)$$

where

$$\begin{aligned} k &= \sqrt{\frac{2\mu}{\hbar^2}(V_0 + E)} \\ \eta &= \sqrt{\frac{2\mu|E|}{\hbar^2}}. \end{aligned} \qquad (4)$$

Let us the model (oversimplified !) for the case of ^{11}Be, which is a one-neutron halo.

We know S_n is about 0.5 MeV, so that $\eta \sim 1/6$ fm^{-1}.

The size of the neutron orbit in ^{11}Be is two times the core size

$R_0 A^{1/3} = 2.67$ fm

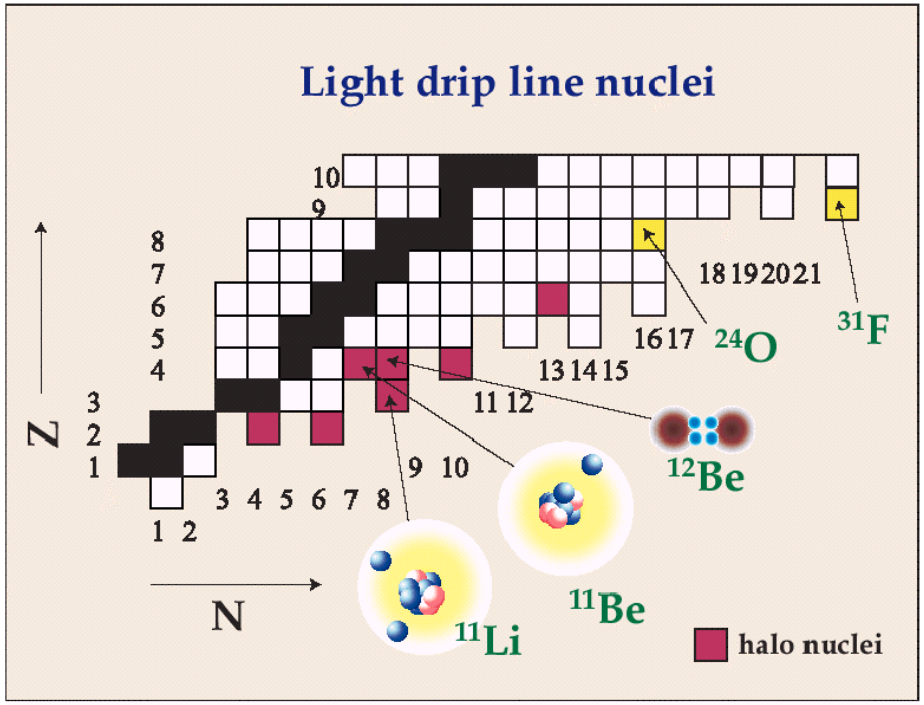

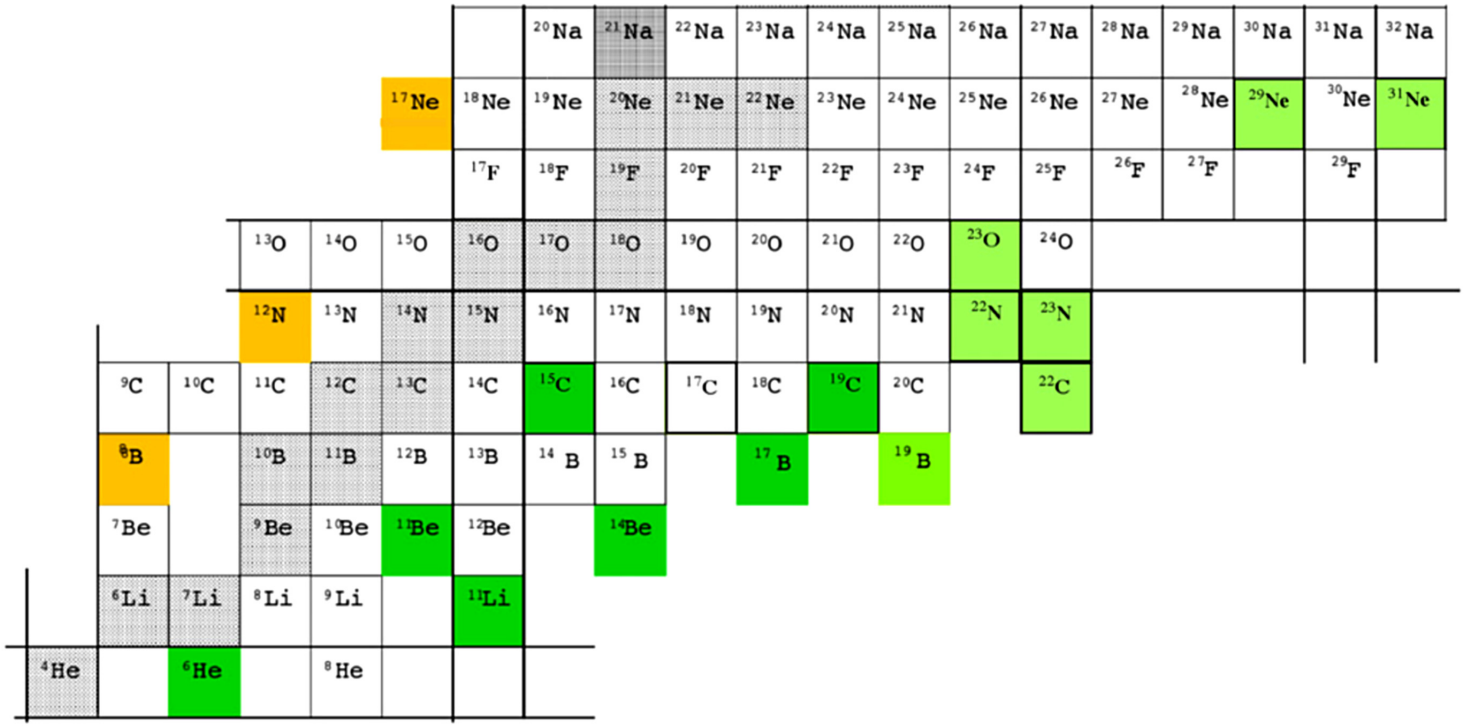

Figure 1.4. Confirmed and suggested halo nuclei. Known neutron halo nuclei are shown by dark green squares and unconfirmed candidates by light green squares. Orange squares show the proton halos. Nuclides only qualify as candidates when significant enhancements of their interaction cross sections are observed (see later). A halo nucleus is treated as confirmed when both enhancement of the cross section and narrow momentum distribution are observed. Reproduced from [7] with permission from Elsevier.

Updated to 2017

IOP Concise Physics

Halo Nuclei

Jim Al-Khalili

Other evidences

• Other experiments which have been historically important, to make the character of halo nuclei evident, are: (i) momentum distributions of projectile fragments, and (ii) electromagnetic dissociation.

These are reviewed in papers e.g. by I. Tanihata.

The idea of the momentum distribution experiments is quite simple. If we hit, e.g., ^{11}Li on a C target at 800 MeV/u we can measure the transverse momentum of the fragments and we find a “double” distribution.

The component with “small width” has a Δp of about 19 MeV/c. From the uncertainty principle

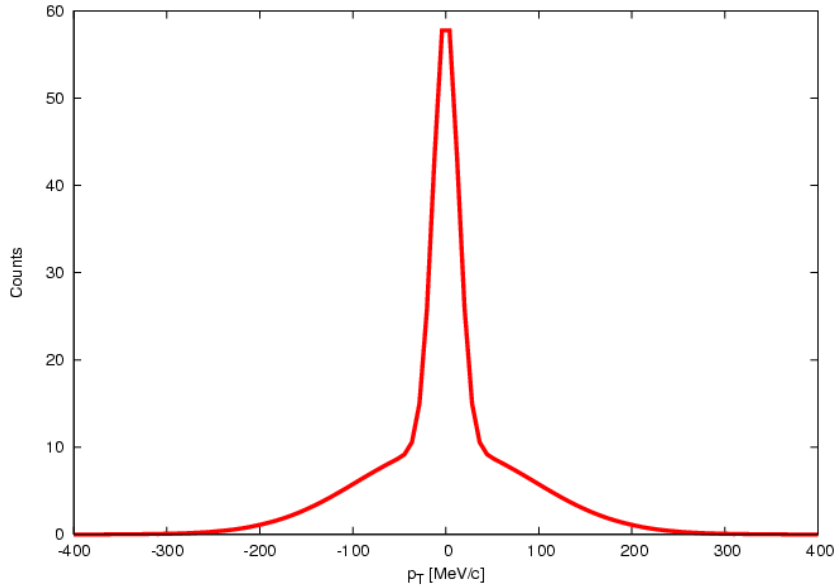

$\Delta x \sim hc/\Delta p \sim 12$ fm,

that is, the narrow component is arising from the halo.

The best-fitted density distribution $\rho(r)$ for ^{11}Li is shown in Fig. 10. For the halo neutrons, 1p or 2s orbits were assumed, and the both fits gave essentially the same distribution as seen in the figure. A difference was seen in the orbital energy, which was ascribed to the centrifugal-barrier effect. It was noted here that the selection of orbital was more or less arbitrary and only the final density distribution had the practical meaning. The obtained density distribution gave the rms radii, $R_{rms}(^{11}\mathrm{Li})$ =3.1 ± 0.3 fm, and R_{rms}(2n) =4.8 ± 0.8 fm for the ^{11}Li nucleus and the halo neutrons, respectively. The size of the ^{9}Li core (R_{rms} ~2.6 fm) turned out to be slightly larger than that of the ^{9}Li nucleus (R_{rms} =2.32 ±0.02 fm), qualitatively consistent with the center-of-mass motion of ^{9}Li core in ^{11}Li.

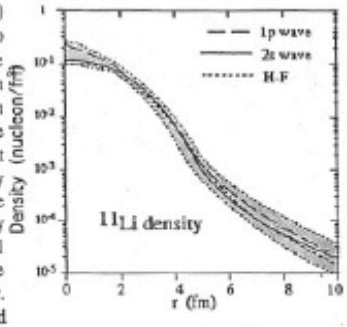

Fig. 10. Density distribution of ^{11}Li deduced from the interaction cross sections. The selection of orbitals, 1p or 1s for the halo neutrons, gave only a minor difference. The shaded area shows the fitting uncertainty. The dotted line shows the H-F model prediction constrained by the last neutron separation energy.

Functional shapes other than the one described above were also investigated: a) Single Gaussian gave no good fit to the data and was definitely inappropriate. b) Gaussian core + Yukawa tail gave also a good fit and the obtained $\rho(r)$ showed essentially the same halo tail but with a slightly higher central density.

Intensive theoretical studies have been performed to understand the structure of these halos by various authors. Bertsch, Brown and Sagawa [19] made a Hartree-Fock calculation by constraining the separation energy of the last occupied orbit. The calculated density distributions are shown in corresponding figures (Fig. 9 and Fig. 10). They show good agreement with the present semi-empirical result. An important implication of the HF calculation is that the long tail of the density distribution mainly arises from the weakly-bound last neutron.

A microscopic model of ^{11}Li was developed by Ikeda, Suzuki and their collaborators [20] by a hybrid model combining a cluster-orbital-shell model with an extended cluster model. The model gave a plausible explanation of the binding mechanism of the three-body system of ^{9}Li+n+n, and both the rms radius and the last-neutron binding energy were consistently reproduced.

4.3 Momentum distributions

Studies of projectile fragmentation at high energy (≥400 MeV/nucleon) shows that the momentum distribution of nucleons inside a projectile nucleus can be determined from the momentum distribution of the projectile fragments. Extending the method used for stripping reactions to many nucleon removal, the width of the P_t distribution* of the projectile fragment is expressed by the separation energy of last neutrons,

$$\sigma^2 = 2u\langle E_s\rangle \frac{A_F(A_F - A_P)}{A_P}, \qquad (4.5)$$

where u is the atomic mass unit and $\langle E_s\rangle$ is an average separation energy of the removed nucleons. It is essentially the same conclusion with the discussion in sec. 4.1.

The transverse momentum distributions of fragments of ^{11}Be and ^{11}Li by carbon target were firstly measured at 790 MeV/nucleon.[3] Figure 11 presents a transverse momentum distribution of (a) ^{10}Be fragment from ^{11}Be + C reaction and (b) ^{9}Li fragment from ^{11}Li + C reaction both at 800A MeV. Both of the data show a very narrow peak on top of another wider peak. The fitting of the momentum distribution by two gaussians gives the width to be σ_{narrow}=25 ± 4 MeV/c and σ_{wide}=109 ± 7 MeV/c for ^{10}Be spectrum. In ^{9}Li, σ_{narrow}= 21 ± 3 MeV/c and σ_{wide}= 80 ± 4 MeV/c. The narrow peaks indicates an existence of neutrons with extremely small momentum fluctuation as expected in the neutron halo. The σ_{wide} is consistent with the momentum fluctuations of usual nucleons.

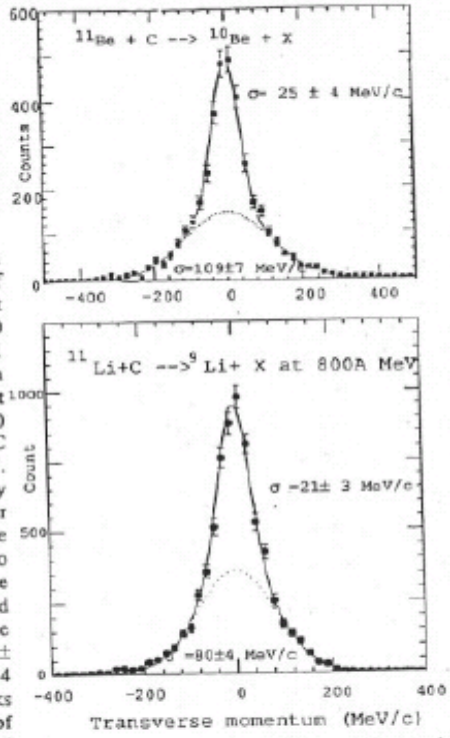

Fig. 11. Transverse momentum distribution of fragments from halo nuclei ^{11}Be and ^{11}Li

* The P_t distribution ($d\sigma/dP_t$) here is defined as,

$$\frac{d\sigma}{dP_x} = \iint \frac{d^3\sigma}{dP_x dP_y dP_{//}} dP_y dP_{//}$$,where $(P_x, P_y, P_{//})$ corresponds to the momentum vector in the Cartesian coordinate (x,y,z) with z being the direction of an incident beam.